Advanced Materials Technologies

ADVANCED MATERIALS TECHNOLOGIES
www.advmattechnol.com

RESEARCH ARTICLE OPEN ACCESS

Lead-Free Bismuth Halide Perovskite Memristors: Low-Voltage Switching and Physical Modeling of Resistive Hysteresis

So-Yeon Kim[1] | Gonzalo Rivera-Sierra[1] | Bitania Shiferaw Mengesha[2] | Benjamin Iniguez[2] | Juan Bisquert[1]

[1]Instituto De Tecnología Química (ITQ), Universitat Politècnica de València- Consejo Superior De Investigaciones Científicas (UPV-CSIC), Valencia, Spain | [2]Department of Electronic and Electric Engineering and Automatics, Universitat Rovira i Virgili, Tarragona, Spain

Correspondence: So-Yeon Kim (skim3@itq.upv.es) | Juan Bisquert (jbisquer@itq.upv.es)

Received: 6 October 2025 | **Revised:** 2 December 2025 | **Accepted:** 17 December 2025

Keywords: conductance-activated quasi-lineal memristor (CALM) | halide perovskites | lead-free perovskite memristor | ReRAM | resistive switching

ABSTRACT

This work reports the resistive switching performance and physical modeling analysis of hysteresis in lead-free all-inorganic mixed halide perovskite memristors. Ag/$Cs_3Bi_2I_{9-x}Br_x$/ITO memristors with I-rich (x = 3) and Br-rich (x = 6) crystallize in a layered trigonal phase and form smooth and uniform films confirmed by XRD, SEM, and AFM analyses. Both devices exhibit reproducible bipolar switching with below 0.3 V SET/RESET voltages, ON/OFF ratios above 10^1, and excellent cycling and retention stability. Crucially, this study provides the first direct experimental validation of the conductance-activated quasi-linear memristor (CALM) framework in bismuth-based halide PSK memristors, showing quantitative agreement between measured and simulated *I–V* hysteresis. Electrical analysis combined with scan-rate–dependent *I–V* physical modeling reveals ion-migration-controlled filament dynamics. I-rich layers form uniform and stable filaments due to stronger Bi–I bonding and lower density of mobile halide vacancies, produced uniform and stable conductive filaments. In contrast, Br-rich memristors exhibit ultralow voltage operations enabled by enhanced vacancy mobility, albeit with slightly broader switching thresholds. These findings demonstrate that compositional engineering in Pb-free bismuth PSK enables a balance between low-voltage operation and stable switching by the incorporation of Br^- ions. The combined experimental-modeling approach establishes a robust lead-free materials platform for next-generation energy-efficient non-volatile memory and neuromorphic electronics.

1 | Introduction

The explosive growth of big-data applications in artificial intelligence (AI) and the Internet of Things (IoT) demands memory technologies that can overcome the scaling and power limitations of conventional flash memory [1, 2]. Memristors have emerged as promising candidates. They offer ultrafast and energy-efficient data storage in a simple metal-insulator-metal (MIM) architecture. Their conductance can be modulated by external stimulus (electrical or optical), enabling parallel in-memory and neuromorphic computation, nociceptor functions, and highly integrated 3D crossbar arrays [3]. These capabilities highlight memristors as building blocks for dense and multifunctional computing hardware [4].

Nevertheless, practical development still requires advances in material discovery, device reliability, and fundamental understanding of ion migration and conduction mechanisms [5]. Such switching is generally attributed to defect-mediated ion migration and filament dynamics. Recently, these processes have been described within physical frameworks such as the conductance-activated quasi-linear memristor (CALM) model [6, 7].

Among active materials, halide perovskites (PSK) are especially attractive for low-power, high-density memristors due to their high light absorption [8], defect tolerance [9], tunable bandgaps [10], and high ion mobility [11]. Their characteristic current-voltage (*I–V*) hysteresis has been widely reported, mostly in lead-based 3D PSK (ABX_3, where A = monovalent cation, B = Pb^{2+}, and X = halide anion) [10]. These systems provide high storage capacity at a fast rate compared to low operating voltages and multifunctionality under electric or optical control. Their compositional flexibility at each crystallographic site further allows tuning of electronic and ionic properties [12]. However, the toxicity and instability of Pb and organic cations remain critical barriers for commercialization, motivating intensive research into Pb-free alternative [13–15].

Bismuth (III)-based PSK are emerging as promising candidates. They offer crystal stability, bandgap tunability, low-temperature fabrication, and durability for multi-functional electronic devices, including memristor, neuromorphic circuits, X-ray detectors, and light-emitting devices [16–20]. Despite this potential, two key gaps remain: (i) lack of systematic memory characterization with compositional engineering, and (ii) the absence of physical modeling and simulation to elucidate their switching mechanisms. Addressing these gaps requires studies that flexibly control memory characteristics through structural and compositional tuning, validated by theoretical insights.

In this work, all-inorganic Bi-based PSK were designed by employing inorganic A-site cations and selectively substituting halide anions to directly compare I-rich and Br-rich compositions. Mixed-halide substitution provides a straightforward route to tune ionic mobility and vacancy concentration. This approach also helps disentangle the distinct roles of iodide and bromide in defect energetics, filament formation, and switching reproducibility. The two compositions studied here represent the iodide-rich and bromide-rich limits of $Cs_3Bi_2I_{9-x}Br_x$, offering a controlled platform to examine how halide substitution governs switching behavior. Previous studies on Pb-based PSK have shown that Br^- incorporation modifies ion migration dynamics compared to I^- [21, 22]. Yet, its systematic role in lead-free bismuth-based PSK remains largely unexplored.

Here, resistive switching performance was systematically investigated, and physical modeling simulations were performed to correlate experimental observations with ion migration-driven filament dynamics. To our knowledge, this is the first comparative study of compositional engineering and physical modeling in bismuth-based lead-free PSK memristors, providing a framework for tunable, energy-efficient memory technologies. Beyond addressing fundamental gaps, these insights provide both a mechanistic understanding and a practical pathway toward scalable integration of lead-free bismuth based PSK memristors into energy-efficient memory and neuromorphic architectures.

2 | Results and Discussion

Memristor devices based on Ag/lead-free halide perovskite (PSK)/ITO/glass structures were fabricated to investigate the resistive switching (RS) characteristics of $Cs_3Bi_2I_{9-x}Br_x$ (x = 3 or 6), as illustrated schematically in Figure 1a. All-inorganic lead-free PSK layers of $Cs_3Bi_2I_{9-x}Br_x$ with I-rich (x = 3) and Br-rich (x = 6) compositions are deposited onto ITO (indium tin oxide) substrates by the spin-coating method. Ag top electrodes are subsequently deposited via thermal evaporation in Figure 1b. The spin-coated PSK films were crystallized via thermal annealing, confirming the formation of the targeted perovskite phases.

Figure 1c shows the X-ray diffraction (XRD) patterns of the pure glass substrate and the lead-free PSK films with I-rich (x = 3) and Br-rich (x = 6) compositions. Detailed each diffraction peaks are also shown in Figure S1. The I-rich film exhibits dominant diffraction peaks at $2\theta \approx 12.59°$, 17.51°, 21.67°, 26.51°, 30.71°, 34.37°, 37.85° and 43.93°, which can be indexed that (010), (002), (110), (003), (022), (004), (122) and (005) plane. These diffraction peaks of the I-rich film are consistent with the previously reported literature, confirming that $Cs_3Bi_2I_6Br_3$ crystallizes in a trigonal structure with space group $P\bar{3}m1$ and a layered configuration [20, 23]. The Br-rich film displays prominent peaks at $2\theta \approx$ 12.65°, 15.49°, 17.79°, 21.95°, 26.85°, 31.07°, 34.95°, 38.27° and 44.59°, corresponding to (010), (011), (002), (110), (003), (022), (004), (122) and (005) plane. Compared to the I-rich diffraction peaks, $Cs_3Bi_2I_3Br_6$ (Br-rich, x = 6) film displays similar diffraction patterns with the main peaks shifted toward higher 2θ values, indicating lattice contraction due to substitution of larger I^- ions with smaller Br^- ions [24, 25]. The observed diffraction peaks match well with the standard reflections of $Cs_3Bi_2I_{9-x}Br_x$ (x = 3 and 6) with mixed halide ions and indicate the layered perovskite-derived phase.

The surface morphology of lead-free PSK films were investigated using atomic force microscopy (AFM) in Figure 1d,e. AFM topography scans were conducted over a $5 \times 5\ \mu m^2$ area, and representative line profiles were extracted across the scanned regions. Both films exhibit densely packed, uniform grain morphologies on the ITO substrates, without notably pinholes. The root-mean-square (RMS) roughness is estimated to be 13.10 nm for the I-rich film (Figure 1d) and 16.92 nm for Br-rich film (Figure 1e), confirming nanoscale roughness with a uniform surface. 3D AFM topography images and roughness profiles are presented in Figure S2. The I-rich film (Figure S2a) shows 10.65 nm RMS roughness, while the Br-rich film (Figure S2d) shows 18.73 nm in the same $5 \times 5\ \mu m^2$ range. Figure S2b,c,e,f shows the cross-sectional and surface field effect scanning emission microscope (FESEM) images of the I-rich and Br-rich films, respectively, both recorded at 50 000 magnifications with a 100 nm scale bar. Both PSK films were well-deposited onto ~135 nm of ITO layers, with an active layer thickness of about 300–400 nm due to the same fabrication processes. The top-view FESEM images shown in Figure S2c,f further corroborate the uniform surface morphology observed in the AFM analysis, confirming the both Br-rich and I-rich films exhibit consistent grain distribution and surface texture. Energy-dispersive X-ray spectroscopy (EDS) mapping was also performed to verify the elemental distribution and halide composition of the PSK films in Figure S3 [26]. The measured atomic ratios for Cs, Bi, I, and Br show clear and consistent trends corresponding to the intended I-rich and Br-rich stoichiometries, further validating the successful compositional control.

The resistive switching (RS) characteristics of Ag/$Cs_3Bi_2I_{9-x}Br_x$ (x = 3 or 6)/ITO devices were investigated in Figure 2. The current-voltage (*I–V*) characteristics of both devices were measured using

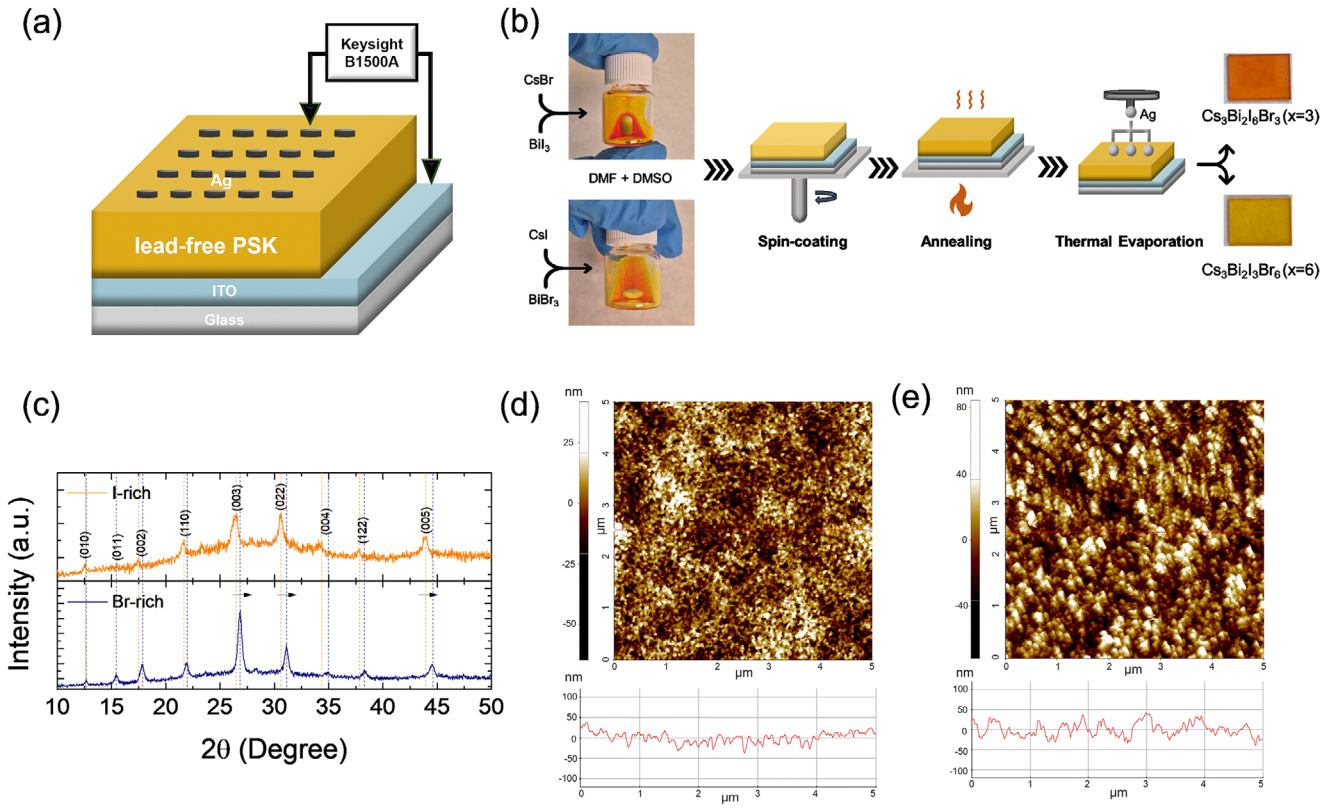

FIGURE 1 | (a) A schematic memristor composed of Ag/$Cs_3Bi_2I_{9-x}Br_x$ (x = 3 or 6)/ITO/glass structure. Keysight B1500A semiconductor analyzer with a probe station system was applied to Ag top electrode and ITO bottom electrode. (b) Schematic fabrication process with photographs of precursor solution and films. (c) X-ray diffraction (XRD) patterns of I-rich lead-free PSK film (orange peaks) and Br-rich lead-free PSK film (blue peaks). (d,e) Atomic force microscopy (AFM) images of lead-free PSK deposited films, each (d) for I-rich film and (e) for Br-rich film.

a semiconductor parameter analyzer equipped with a probe station. The devices employed Ag as the top electrode and ITO as the bottom electrode in a typical metal-insulator-metal (MIM) stacking memristor structure. Voltage sweeps of 0 V → +1 V → 0 V → −1.5 V → 0 V were applied at a scan rate of 100 V/s under a compliance current of 1 mA to prevent excessive current flow. When the compliance current was reached, the current returned to its original resistance state.

Both devices showed reproducible bipolar RS properties over 30 consecutive sweep cycles in Figure 2a for the I-rich memristor and Figure 2d for the Br-rich memristor. During the initial sweep, an electroforming step appeared around +0.5 V to stabilize the sequent switching behavior, confirming the typical conductive filamentary pathway formation [16, 27]. The positive bias region corresponds to the SET process, wherein the device transitions from a high resistance state (HRS, OFF state) to a low resistance state (LRS, ON state). The RESET process occurs under negative bias polarity, resulting in typical butterfly-shaped *I–V* curves. The SET and RESET voltages were extracted from each transition in the 30 consecutive cycles, excluding the initial forming step. In the I-rich ($Cs_3Bi_2I_6Br_3$) memristor, the SET/RESET voltages were plotted as statistical histograms in Figure 2b. The SET voltage was centered at +0.27 V (μ_{set}) and the RESET voltage at −0.17 V (μ_{reset}). Both exhibit narrow distribution with small standard deviations ($\sigma < 0.03$), indicating stable switching thresholds at low operating voltages. Box plots in Figure 2c show the resistance distributions at a read voltage of +0.10 V. The average values of HRS, LRS, and ON/OFF ratio were indicated to 3.27×10^3 Ω, 1.39×10^2 Ω, and 2.35×10^1 Ω, respectively, which is sufficient for reliable memory operation.

Figure 2d–f presents the resistance state distributions of the Br-rich ($Cs_3Bi_2I_3Br_6$) memristor obtained using the same procedure with the I-rich memristor. The average values of SET and RESET voltage were at +0.17 and −0.17 V, respectively, accompanied by a small standard deviation between 0.03 and 0.06 in Figure 2e. Compared to the I-rich memristor, the increase of Br components enables the device operate with the lower operating voltages from +0.27 to +0.17 V, suggesting that the incorporation of Br content lowers the energy barrier for halide ion migration due to their lower activation energy [21, 22]. The resistance distributions confirm that the mean value of ON/OFF ratio was 1.94×10^1 Ω with the average HRS at 1.94×10^3 Ω and the average LRS at 1.05×10^2 Ω in Figure 2f, which is still adequate for readout margins.

Apart from a slight difference in operating voltage, both memristors with mixed halide ions demonstrated performance as low-energy consumption devices, which is a key factor for electronic applications and reflects the facile and fast ion migration properties of halide perovskites-based memristors [5, 28]. These results suggest that compositional engineering in all-inorganic lead-free bismuth based PSK provides an effective approach to tune the balance between resistive switching properties and energy efficiency in memristors.

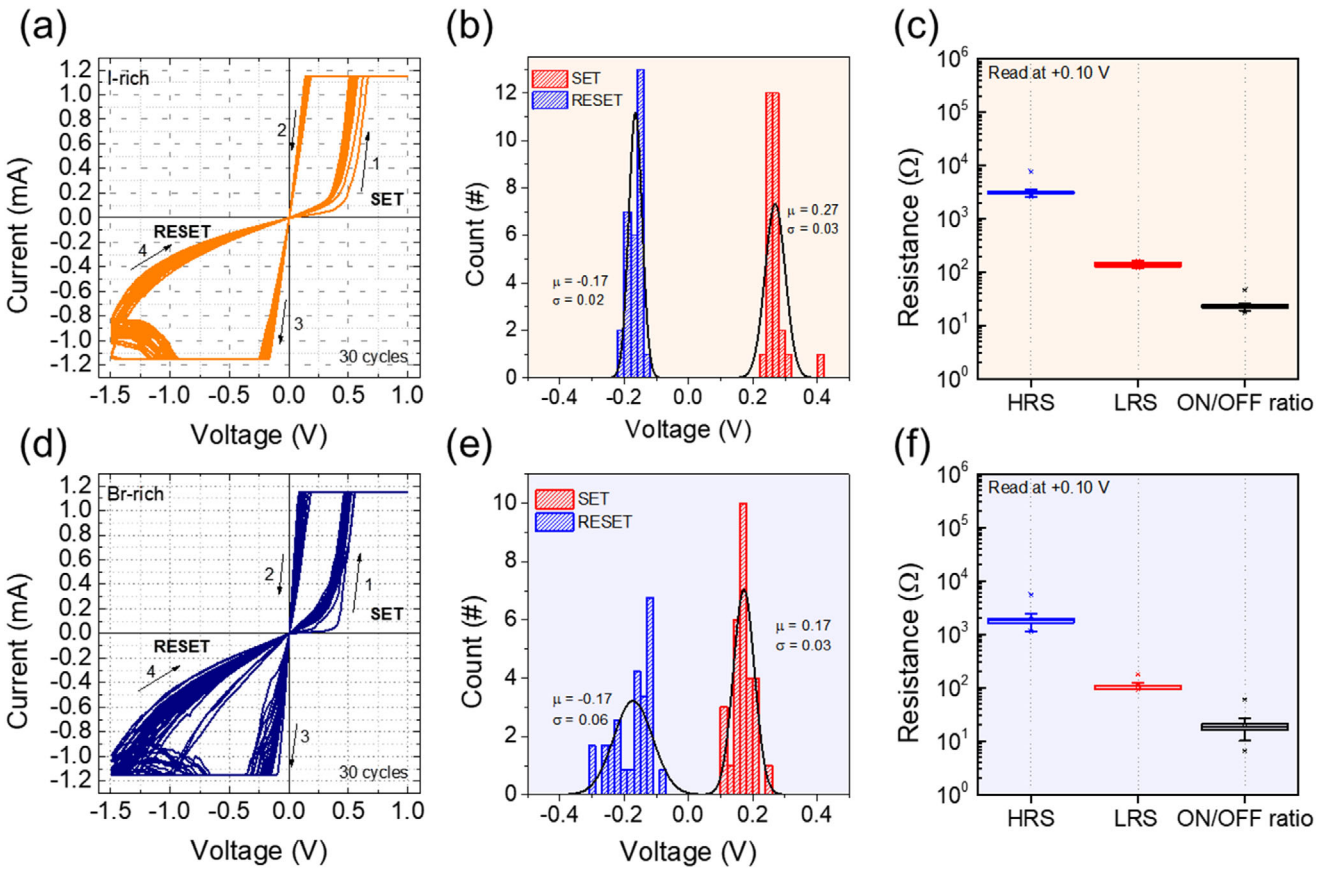

FIGURE 2 | Current-Voltage (*I–V*) memristive characteristics of the Ag/$Cs_3Bi_2I_{9-x}Br_x$ (x = 3 or 6)/ITO memristors. (a–c) $Cs_3Bi_2I_6Br_3$-based memristor (I-rich PSK, x = 3) and (d–f) $Cs_3Bi_2I_3Br_6$-based memristor (Br-rich PSK, x = 6). The devices were applied with the bias voltage of +1.0 V for forming and SET processes and −1.5 V for RESET processes under a compliance current of 10^{-3} A. *I–V* curves for 30 cycles, including the forming step of (a) I-rich and (d) Br-rich memristor. Switching statistical histograms of SET and RESET voltages with a single-Gaussian fits obtained in (b) I-rich and (e) Br-rich devices, where the extracted mean (μ) and the standard deviation (σ) are annotated. Box-plots of HRS, LRS, and ON/OFF ratio read at +0.10 V obtained from (c) I-rich and (f) Br-rich memristor.

Figures 3 and S4 show the cell-to-cell reproducibility of the lead-free PSK memristors. All 50 different memristor cells were fabricated under identical processing conditions and evaluated via voltage sweeps ranging from +1.0 to −1.5 V at 100 V/s with the read voltage fixed at +0.10 V. The *I–V* curves from 50 individual cells were collected for both I-rich (Figure 3a–c) and Br-rich (Figure 3d–f) memristors. The initial forming processes required to create the conductive pathways for stable repetitive switching were extracted from all 50 memristors and compiled into a single plot, as shown in Figure 3a for I-rich and Figure 3d for Br-rich memristors. To further analyze the initial switching behavior, the forming voltages were extracted by identifying the transition point where the resistance switched from the initial HRS to LRS. Statistical distributions of forming voltages (Figure S4a) reveal that Br-rich memristors require lower forming voltages (+0.37 V) compared to their I-rich counterparts (+0.64 V), with a narrow spread (±0.08 V) for both device types. This trend agress with the single cell results in Figure 2 and reflects the role of Br^- incorporation in reducing ion migration barriers. This observation is consistent with previous reports on mixed-halide perovskites (e.g., $CH_3NH_3PbI_{3-x}Br_x$), where Br^- incorporation lowers the ionic migration barrier of vacancies compared to I^-, thereby facilitating conductive pathway formation at reduced bias fields [21, 22].

In our lead-free PSK memristors based on $Cs_3Bi_2I_{9-x}Br_x$, Br incorporation is therefore expected to enhance ionic mobility and increase the density of mobile vacancies, leading to reduced voltage thresholds for filament initiation. Such low-voltage operation is particularly advantageous for energy-efficient resistive switching, suggesting that compositional engineering of PSK provides a viable strategy toward lower-power consumption memory devices and neuromorphic computing applications. Figure S4b,c illustrates the resistance distributions of HRS and LRS at the first forming step for I-rich and Br-rich memristors, respectively. Both devices exhibit a clear separation between the LRS and HRS at all switching first steps under a read voltage of +0.10 V, indicating the initiation of resistive switching through an internal resistance change. For the I-rich memristor, the box plot deviation during the forming process exceeds 10^3 Ω, while Br-rich memristors show narrower distributions of both LRS and HRS, yielding a lower ON/OFF ratio due to the ion migration effects [17, 29]. This reduction in switching contrast may be attributed to the enhanced ionic mobility introduced by Br incorporation. The increased halide ion conductivity and vacancy density can promote the formation of more conductive or leaky filament paths, thereby decreasing the resistance contrast between ON and OFF states. While this supports lower operating voltages, it results in a trade-off in switching clarity. This interpretation is consistent

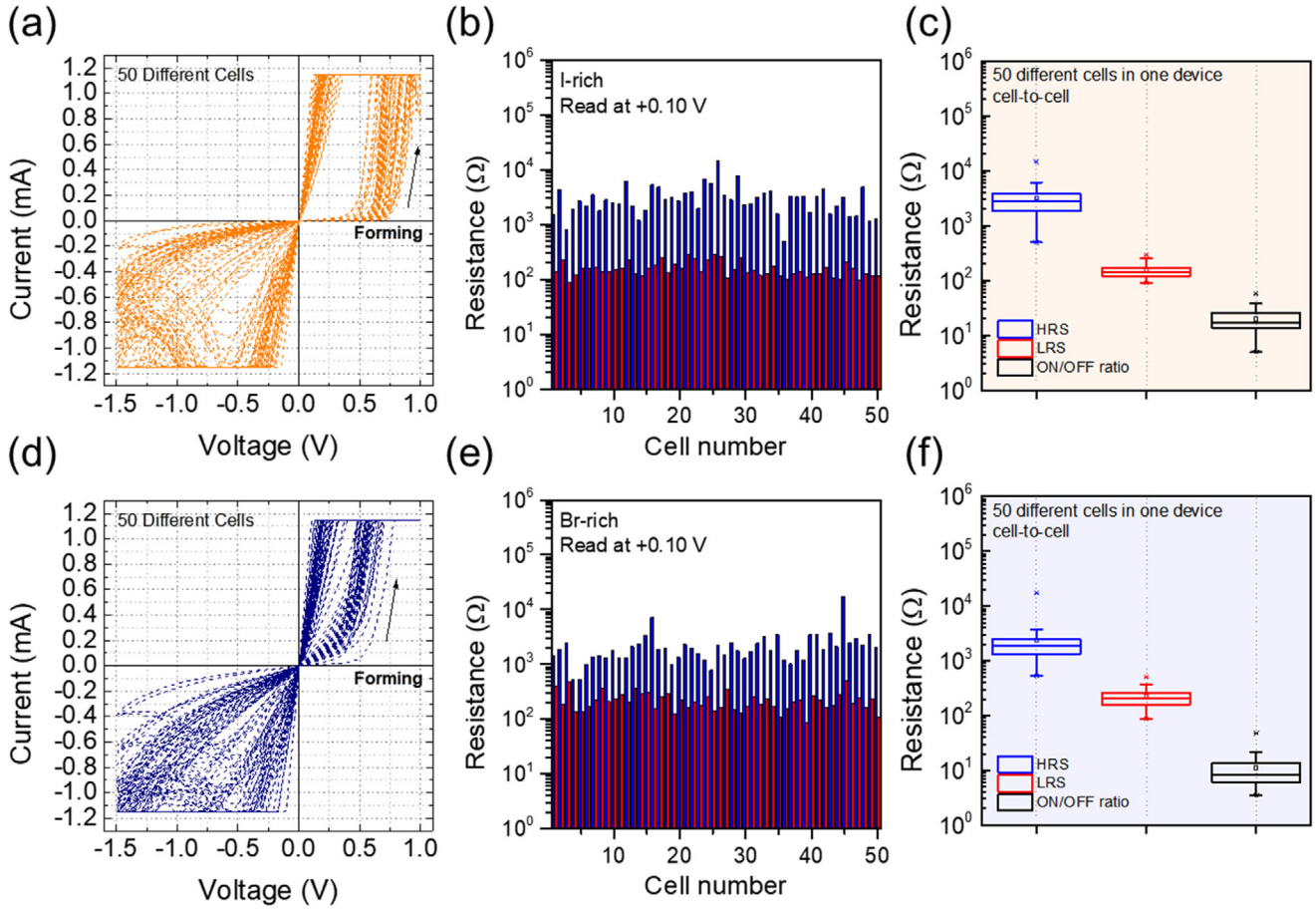

FIGURE 3 | Reproducibility test of lead-free PSK based memristors. Cell-to-cell reproducibility data across each 50 cells measured in a single (a–c) $Cs_3Bi_2I_6Br_3$-based memristor (I-rich PSK) and (d–f) $Cs_3Bi_2I_3Br_6$-based memristor (Br-rich PSK). DC voltage sweeps of the Ag/lead-free PSK/ITO device were performed with the bias voltage of +1.0 V for forming and SET processes and −1.5 V for RESET processes with a compliance current of 10^{-3} A. All resistance values were read at +0.10 V. Collected *I–V* curves obtained at the initial forming steps from 50 individual cells for (a) I-rich and (d) Br-rich devices. The resistance values of HRS, LRS, and ON/OFF ratio at random sweep after forming process were statistically analyzed and presented as box-plot of (b,c) I-rich and (e,f) Br-rich devices.

with previous studies on halide perovskites, where increased Br content in Pb-based PSK has been shown to enhance ion transport but also affect switching sharpness due to filament diffusion [21].

Figure 3b,c,e,f presents the cumulative probability of resistance states at the randomly selected sweep after forming processes read at +0.10 V, showing the distributions of the OFF state (HRS) and ON state (LRS) for the I-rich and Br-rich memristors, respectively. The average values of HRS, LRS, and ON/OFF ratio were observed with 3.21×10^3 Ω, 1.57×10^2 Ω, and 1.97×10^1 Ω for I-rich memristors and 2.34×10^3 Ω, 2.21×10^2 Ω, and 1.11×10^1 Ω for Br-rich memristors. In the subsequent *I–V* curves after the forming steps, most cells showed reduced resistance and lower operating voltages compared to the initial sweep, reflecting the establishment of the conductive pathways characteristic of the typical forming process. Beyond the pronounced initial changes during the formation process, no significant differences were observed in the subsequent resistance states between the I-rich and Br-rich memristors. This indicates that both devices formed stable conductive pathways capable of repeatable switching. All 50 cells maintained stable resistive switching over repeated cycles, demonstrating device reliability essential to practical memory integration.

To investigate the cycle durability of the memristors, DC endurance tests were conducted as shown in Figure 4 for Ag/lead-free PSK/ ITO memristors. Each device was operated with a SET voltage of +1.0 V and RESET voltage of −1.5 V under a compliance current of 1 mA, while resistance was read at +0.10 V using a scan speed of 100 V/s. Results for I-rich and Br-rich memristors are shown in Figure 4a,b, respectively. Both memristors retained clear separation between the high resistance state (HRS) and the low resistance state (LRS) for over 10^3 consecutive switching cycles without obvious degradation, confirming stable bipolar resistive switching behavior. Occasional scattered resistance values were observed, which are attributed to stochastic ion migration event. However, these did not significantly affect the overall resistance distributions or endurance performance. The average ON/OFF ratios extracted from the cycling tests were approximately 2.54×10^2 for the I-rich memristor and 1.34×10^1 for the Br-rich memristor. Although the ON/OFF ratio of the devices ranges from approximately 10^1 to 10^2, the statistical distributions in Figures 2–4 clearly show

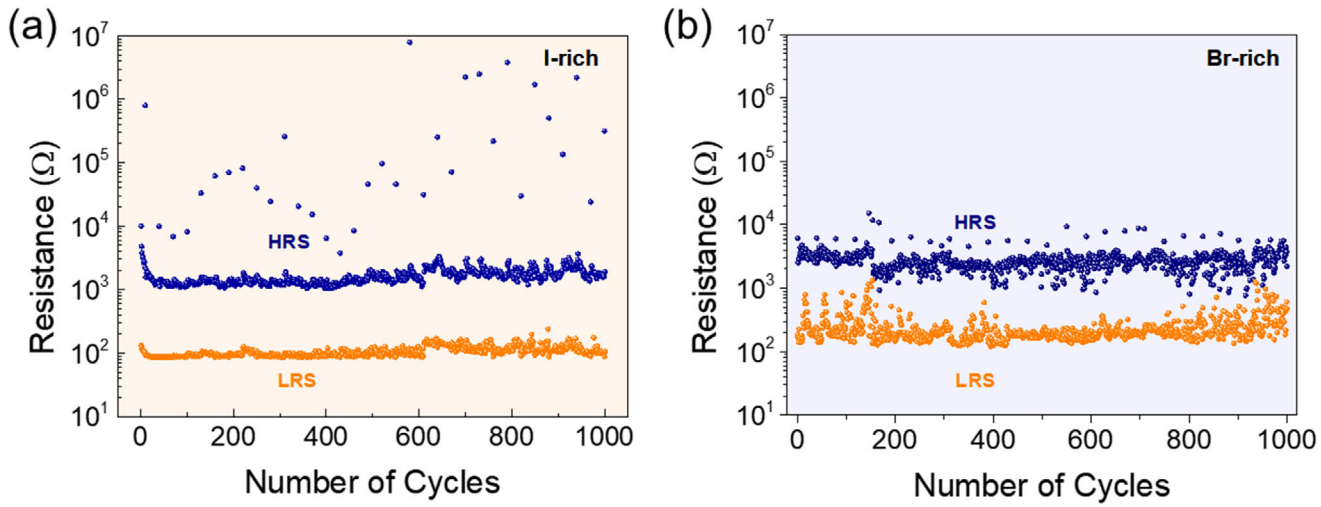

FIGURE 4 | Cyclability test (endurance) of the Ag/lead-free PSK/ITO device measured with the bias voltage of +1.0 V for SET process and −1.5 V for RESET process and compliance current of 10^{-3} A. All reading voltage was +0.10 V, and scan speed for applied voltages was 100 V/s. (a) $Ag/Cs_3Bi_2I_6Br_3/ITO$ (I-rich) and (b) $Ag/Cs_3Bi_2I_3Br_6$ (Br-rich).

that the HRS and LRS remain well separated without overlap throughout the cycling tests. This degree of state separation is sufficient for reliable resistive-state discrimination under the applied read voltage. Moreover, such moderate ON/OFF ratios are also fully compatible with neuromorphic and synaptic applications, where analog-like and gradual conductance modulation is more critical than achieving extremely large resistance contrasts [11, 17, 30]. While both are sufficient for readout margins, the reduced ratio in the Br-rich device is consistent with earlier observations and can be attributed to enhanced ionic mobility. Increased halide conductivity and vacancy density in Br-rich compositions may lead to more conductive or partially formed filament paths, reducing the resistance contrast between ON and OFF states. The long-term retention characteristics were further evaluated by monitoring the HRS and LRS over a period of 103 s under ambient conditions, as shown in Figure S5. Additional quantitative parameters extracted from the devices are summarized in Table S1. Measurements were performed under the same operating conditions as the cyclability test. Both memristors maintained stable resistance states with negligible drift throughout the duration, confirming excellent data retention behavior suitable for non-volatile memory applications.

To further investigate the role of ion dynamics in resistive switching, scan rate-dependent *I–V* characteristics were analyzed for both I-rich and Br-rich memristors, as shown in Figure S6a,b. In both devices, the switching window and current levels varied significantly with the applied voltage sweep rate from 1000 V/s (fastest) to 10 V/s (slowest). A slower scan rate facilitated ionic redistribution, leading to more pronounced hysteresis, while faster sweeps limited ionic motion and produced narrower switching windows. These trends suggest a strong influence of dynamic processes such as ion migration and accumulation under different field or time-scale conditions, confirming the time-dependent nature of resistive switching in these lead-free PSK memristors [6, 7].

To support the experimental results with theoretical insights, the scan rate dependence was further analyzed using the conductance-activated quasi-linear memristor (CALM) framework [7, 31]. In this model, the device response is described as a dynamic transition between two well-defined Ohmic conductance states; a low conductance state g_L and a high conductance state g_H. The transition is governed by a state variable x, which physically represents the fraction of active conduction pathways, i.e, the degree of filament formation respect to the maximum. The total current under an applied bias V is thus expressed as

$$V = R_s I_{tot} + u \tag{1}$$

$$I_{tot}(u) = [g_L + (g_H - g_L)\,x]\,u + C_m \frac{du}{dt} \tag{2}$$

where u denotes the internal voltage within the device, R_s the overall series resistance of the device and the measurement configuration and C_m the dielectric geometrical capacitance. Since both contributions are negligible in our devices ($R_s \ll$ and $C_m \ll$), we approximate $u \approx V$. This simplification allows us to use the external applied voltage as the driving variable in the model. The transition between g_L and g_H is governed by the memory variable x, which varies continuously between 0 (OFF state) and 1 (ON state) according to the applied voltage. The steady-state value of this variable, $x_{eq}(u)$, follows a sigmoidal activation function characterized by a steepness parameter V_m and an onset parameter V_x

$$x_{eq}(u) = \frac{1}{1 + e^{-\frac{u - V_x}{V_m}}} \tag{3}$$

indicating when and how the CFs would form in our device with respect to the applied voltage, assuming an ideal stationary situation. The time-dependent dynamic evolution of x is described by a first-order relaxation process toward x_{eq}, with a characteristic voltage-dependent relaxation time

$$\tau_x(u)\frac{dx}{dt} = x_{eq}(u) - x \tag{4}$$

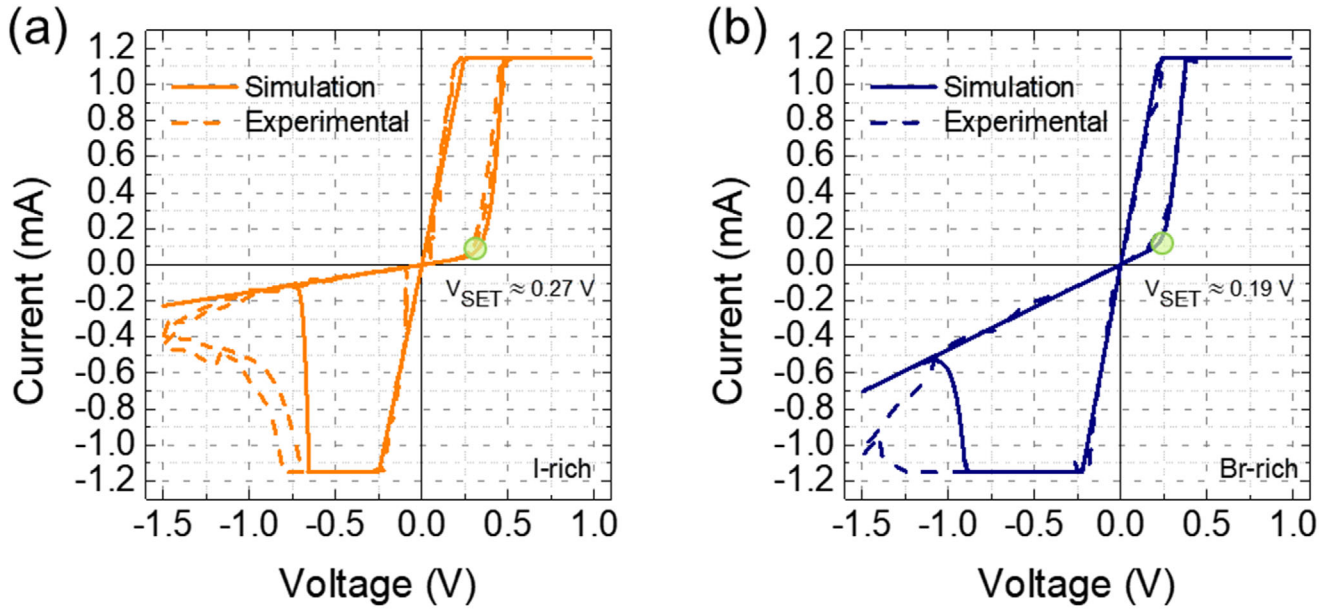

FIGURE 5 | Graphical representation of the theoretical model fitting at a fixed sweep rate of 10 V/s for both memristors under study. Solid lines correspond to simulated curves and dashed lines to experimental data, with (a) the I-rich device shown in orange and (b) the Br-rich device in blue. In both graphs, a green marker indicates the voltage at which the SET process is initiated. The fitting parameters are summarized in Table S2.

$$\tau_x(u) = \frac{\tau_{max} + \tau_{min_{OFF}} e^{-\frac{u-V_{OFF}}{V_-}}}{1 + e^{-\frac{u-V_{OFF}}{V_-}}} - \frac{\tau_{max} + \tau_{min_{ON}}}{1 + e^{-\frac{u-V_{ON}}{V_+}}} \quad (5)$$

This temporal variable will vary as a function of the applied voltage, according to the specific mobility and migration barrier properties of the ionic species in the active material of the device.

The functional form of τ_x introduces a set of parameters that capture the activation/deactivation kinetics of the system. Specifically, V_{ON} and V_{OFF} represent the activation and deactivation voltages, while V_+ and V_- define the steepness of the activation and deactivation branches, respectively. The parameters τ_{max}, $\tau_{min_{ON}}$, and $\tau_{min_{OFF}}$ correspond to the maximum and minimum relaxation times for activation and deactivation. Altogether, this description results in a characteristic non-monotonic ('mountain-shaped') dependence of the relaxation time, capturing the kinetics of filament nucleation and rupture. A schematic illustration of the CALM framework is provided in Figure S7.

In Figure 5, the CALM fitting reproduces the experimental *I–V* characteristics with high fidelity. This agreement provides strong validation that the switching dynamics of both I-rich and Br-rich memristors can be quantitatively captured within the CALM framework. The fitting consistently reinforces the experimentally observed trend toward lower SET voltages in Br-rich compositions compared to I-rich ones. The fitting results across multiple sweep rates for each memristor are presented in Figures S8 and S9, while the functional forms of the relaxation time τ_x and the steady-state memory variable x_{eq} are illustrated in Figure S7. The exacted fitting parameters, summarized in Table S2, highlight systematic differences between I-rich and Br-rich compositions. Overall, the simulated curves reproduce the experimental response with high fidelity.

From further analysis of the fitting results, it is observed that the Br-rich memristor requires a shorter overall time to initiate the SET process compared to the I-rich memristor. Although the minimum characteristic time under positive bias ($\tau_{min_{ON}}$) is smaller for the I-rich device ($\tau_{\min ON}, I < \tau_{\min ON}, Br$), it reflects the ionic response time after activation rather than the initiation of the SET process itself. As in the experimental results, the Br-rich memristor reaches this low-relaxation time regime at a lower voltage of ($V_+ = 25\ mV$), than the I-rich memristor ($V_+ = 30\ mV$), indicating that the system enters the fast-switching regime at a lower voltage in Br-rich devices, consistent with a lower ionic migration barrier. This behavior is directly manifested in the reduced SET voltage measured in the Br-rich curves, as already discussed and experimentally illustrated in Figure 2. In contrast, during RESET, the Br-rich device exhibits a longer response time, and the applied current compliance limits the accuracy of determining the onset voltage. The theoretical RESET onset (could be estimated with the parameter V_{OFF}) is approximately –0.40 V for Br-rich, whereas it is closer to –0.25 V for I-rich, with the latter being more sharply defined due to the reduced compliance influence. This difference explains the broader experimental distribution of RESET voltages observed for Br-rich devices (Figure 2).

Theoretical and parametric analysis can support these experimental trends, highlighting the interplay between halide composition and ionic switching dynamics. The fitting results show that the minimum relaxation times are larger for Br-rich devices compared to I-rich ones ($\tau_{\min ON}$ and $\tau_{\min OFF}$ for I-rich are smaller than those for Br-rich, Table S2). This might appear contradictory to the observed lower SET voltage in Br-rich devices. However, the SET voltage is strongly governed by the

migration energy barrier, which has been consistently reported to be lower for Br^- than for I^- [22]. As a result, the activation of ionic migration occurs at a reduced voltage in the Br-rich case, as confirmed by the experimental curves. In the model fits, this is reflected in the steeper decrease of the relaxation time during the SET transition (V_+ is smaller in Br-rich than in I-rich), where the system reaches the small relaxation-time regime (corresponding to barrier crossing and the onset of ionic migration) earlier for Br^- than for I^-. Thus, the apparent discrepancy is resolved: while Br^- exhibits longer intrinsic relaxation times (lower mobility), the lower migration barrier ensures that SET switching occurs at smaller applied voltages, consistent with both experimental observations and theoretical modeling.

These results represent the first adaptation of such a theoretical framework, CALM to lead-free bismuth-based PSK memristors for a direct comparison between simulated and experimental dynamic switching behavior. Describing the ionic boundary evolution, which directly governs the operating voltage, shifts observed under different scan rates. The excellent agreement between measured and simulated curved confirms that time-dependent ionic redistribution, captured by the evolution of the state variable x and its dynamics, is the dominant mechanism governing RS in these devices.

Another central aspect of the CALM framework is that memristors switch between two well-defined and fully Ohmic conductance states, according to Equation (2). Hence, the I–V characteristics of Ag/$Cs_3Bi_2I_{9-x}Br_x$ (x = 3 or 6)/ITO memristors were analyzed using double-logarithmic plots in Figure 6 in conjunction with the electrode-type and size dependence of resistance in Figures S10 and S11. The forming steps previously shown in Figure 3 revealed abrupt current changes, indicating the formation of typical conductive filaments (CFs) in the PSK active layer. To further verify that the composition-dependent switching characteristics originate from intrinsic ionic processes rather than electrode-specific effects, control devices with an inert Au electrode were also examined in Figure S10. Although the Au-based devices required slightly higher operating voltages, the characteristic trend in which Br-rich devices switch at lower SET voltages than I-rich devices remained fully preserved. This consistency confirms that halide ions/vacancies migration dominantly governs the switching behavior, independent of the top electrode [5]. Figure S11 further confirms that both I-rich and Br-rich devices exhibit negligible area dependence in HRS and LRS, indicating localized CF switching rather than interface-type mechanisms [5, 32]. The operating conduction mechanisms of the CFs were clarified by analyzing the I–V curves, and both devices showed similar conduction mechanisms with multi-steps in Figure 6. Importantly, both the low-current and high-current branches in Figure 6 exhibit a slope $\alpha \approx 1$, providing the first direct experimental evidence of the CALM model in bismuth-based PSK memristors. All these features are crucial for both the reproducibility of the devices and the validity of the theoretical model.

At the initial low bias region (step 1) in HRS, the slope $\alpha \approx 1$ indicates Ohmic transport through the pristine PSK matrix, where the current increases linearly with the applied bias [33]. This regime reflects electron injection and drift before any significant ionic rearrangement. As the bias increases at step 2 and 3, the slope rises above $\alpha \approx 2$ to 5, making a transition regime where halide vacancies/ions become increasingly active [16, 34, 35]. In this stage, local ionic redistribution lowers the effective barrier for conduction and promotes the nucleation of the conductive filaments. After reaching the compliance limit, the filaments are established, and the LRS state stabilizes again with Ohmic conduction ($\alpha \approx 1$), although with much smaller resistance, along well-formed CFs from the SET processes.

Under negative bias, the RESET processes through steps 5–7. Immediately after bias reversal, $\alpha \approx 1$ persists along partially intact CFs. At intermediate state with increasing bias, the slope temporarily rises ($\alpha \approx 2$), indicating a transition regime where the filaments begin to rupture. At higher negative bias in step 7, the slope returns to $\alpha \approx 1$ as the CFs are fully dissolved via halide vacancies redistribution, finally restoring the HRS, OFF state. This return to Ohmic transport after filament dissolution further supports the CALM description, suggesting that both the ON and OFF states are governed by quasi-linear Ohmic conduction channels, with dynamic contributions from ion migration processes with halide vacancies [36, 37].

3 | Conclusion

In summary, all-inorganic lead-free bismuth mixed halide perovskites (PSK)-based memristors demonstrated as a robust platform to tune resistive switching (RS) characteristics for multifunctional memory applications. Both I-rich (x = 3) and Br-rich (x = 6) of Ag/$Cs_3Bi_2I_{9-x}Br_x$/ITO memristors exhibited stable bipolar RS behavior with sub-0.3 V SET/RESET voltages, high reproducibilities, and excellent endurance/retention. Combined structural (XRD, SEM, and AFM) and electrical characterizations, together with physical modeling and simulations, revealed that compositional engineering directly modulates halide defect chemistry and ion migration dynamics in bismuth-based lead-free PSK systems. I-rich (x = 3) layers with stronger Bi-I bonding supress vacancy mobility and promote uniform, stable filament formation, while Br^- ion incorporation lowers defect migration barriers, enabling ultralow voltage operation but with slightly broader switching distributions. Double-logarithmic I–V analysis further demonstrated Ohmic conduction in both the low- and high-current branches, providing the first direct experimental validation of the conductance-activated quasi-linear memristor (CALM) framework in bismuth-based PSK memristors. This confirms that both ON and OFF states are governed by quasi-linear conduction channels, mediated by halide vacancy dynamics. These experimental trends are consistent with memristor physical modeling based on ion migration models, which confirms the critical role of ion migration controlled filament dynamics. This study demonstrates that compositional engineering serves as an effective route to balance low-operating voltages and RS stability in lead-free bismuth PSK-based memristors. Given the limited systematic studies on bismuth-based lead-free PSK memristors, this work offers the first experimental-modeling framework for them, providing a foundation for next-generation, multifunctional, energy-efficient memory and neuromorphic electronic systems.

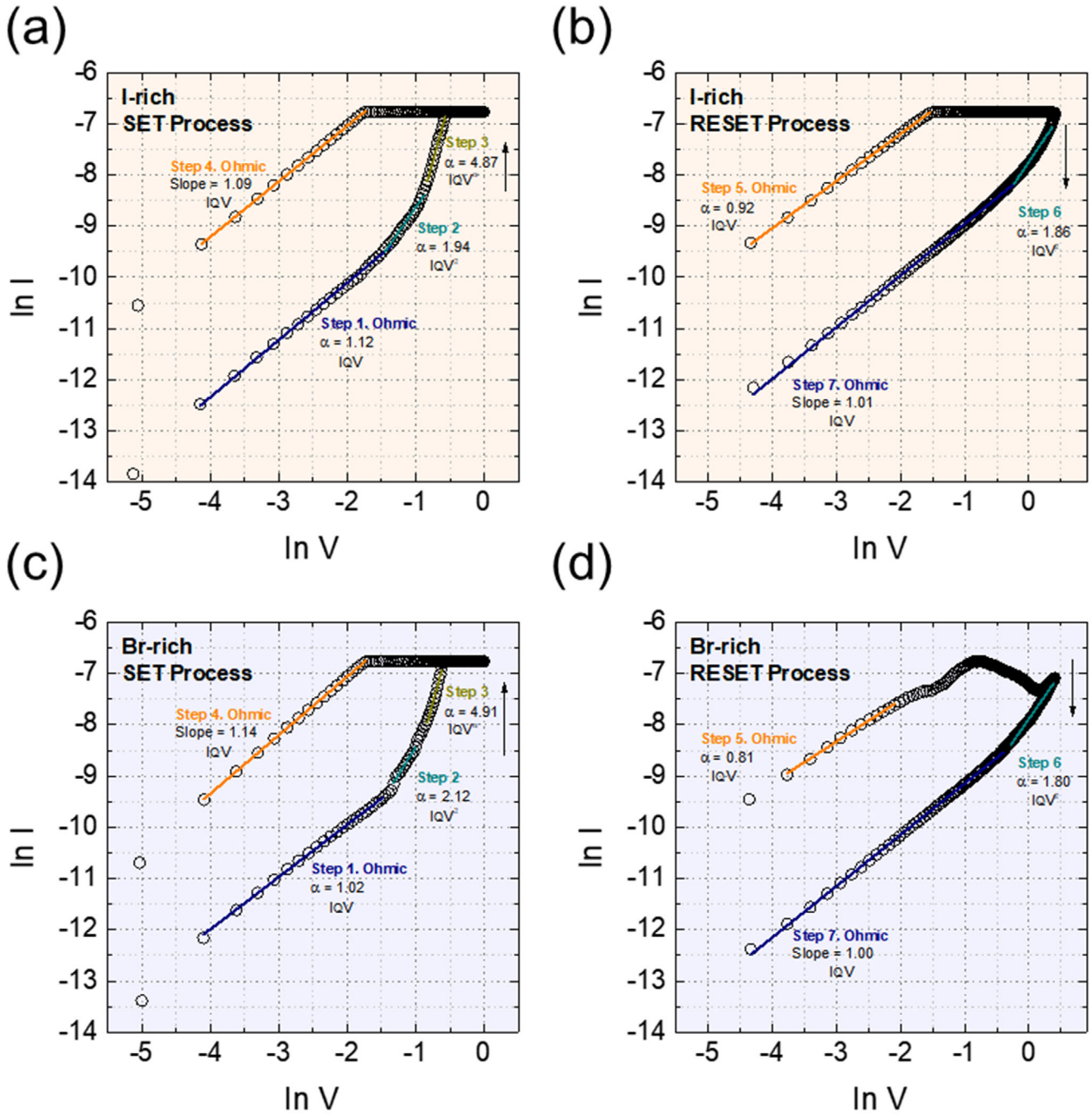

FIGURE 6 | Double natural logarithmic *I–V* plots of Ag/lead-free PSK/ITO memristors used to analyze conduction mechanisms. ln I-ln V plots for I-rich device during (a) SET process and (b) process and for Br-rich device during (c) SET process and (d) process. Linear fittings identify each conduction step with the extracted slope α indicated.

4 | Experimental Section/Methods

4.1 | Materials for Lead-Free All-Inorganic Mixed Halide Perovskite

Cesium Iodide (CsI, 99.9%, Thermo Scientific Chemicals), cesium bromide (CsBr, 99.999%, Sigma–Aldrich), bismuth (III) iodide (BiI_3, 99%, Sigma–Aldrich), bismuth (III) bromide ($BiBr_3$, ≥98%, Sigma–Aldrich), *N,N*-dimethylformamide (DMF, anhydrous ≥99.8%, Avantorsciences), dimethyl sulfoxide (DMSO, ≥99.7%, Sigma–Aldrich) and diethyl ether (anhydrous, ≥99.8%, Avantorsciences) were purchased and used with no further purification.

4.2 | Preparation of the Precursor Solution Based on Halide Perovskite

CsBr and BiI_3 were mixed with a molar ratio of 3:2 for $Cs_3Bi_2I_6Br_3$ (I-rich PSK) in DMF:DMSO (v/v %, 7:3). CsI and $BiBr_3$ were dissolved and totally mixed in DMF:DMSO (7:3) solvent with the molar ratio of 3:2 to prepare the precursor solution of $Cs_3Bi_2I_3Br_6$

(Br-rich PSK). The precursor solution was stirred with a magnetic stirrer until the powder precursors were completely dissolved before deposition.

4.3 | Fabrication of the Memristor Device

Indium tin oxide (ITO)-coated glass substrates were cleaned with detergent in deionized water, acetone, and isopropanol, each for 15 min with sonication. The cleaned ITO substrates were UVO-treated for 30 min prior to deposition. Before the fabrication of the thin perovskite layer onto ITO, the precursor solution was filtered using a PTFE-H syringe filter with a pore-size of 0.22 μm. The filtered precursor solution of 30 μL was dripped onto ITO substrates and spin-coated with a two-step accelerated coating process at 1000 rpm for 10 s and 5000 rpm for 30 s. While spinning at second spinning step, 0.3 mL of diethyl ether was dripped onto the wet film. The as-spun film was annealed at 100°C for 15 min on a hot plate. A 100 nm-thick top Ag electrode was deposited on the annealed film by thermal evaporation using a custom-built evaporator (TVP, Thermal Vacuum Projects S.L.). A dot-shaped shadow mask with variable diameter sizes of 100, 200, and 400 μm was used.

4.4 | Characterizations

X-ray diffraction (XRD) patterns were obtained by an X-ray diffractometer (CUBIX XRD DY0822 X-ray diffractometer) with Cu Kα radiation (wavelength = 1.54056 Å) from PANalyrical Ltd. The XRD data were collected in the 2θ range from 10° to 50° with a step scan size of 0.02°. Field Emission scanning electron microscope (FESEM) (ULTRA 55, ZEISS) was used for investigating cross-sectional film images. Surface roughness was investigated using an atomic force microscope (AFM, Multimode 8, BRUKER) with tapping mode. All electrical properties were characterized with B1500A KEYSIGHT source meter equipped with a probe station. The physical modeling was performed by Simscape from Simulink and a block simulator tool from MatLab.

Acknowledgements

This work was supported by Grant No. EUR2022-134045 funded by MICIU/AEI/10.13039/501100011033 and by European Union NextGenerationEU/PRTR. S.-Y.K., G.R.-S., and J.B. also thank the European Research Council (ERC) via Horizon Europe Advanced Grant Agreement No. 101097688 ("PeroSpiker"). Additional instituional support from the Severo Ochoa Excellence Program CEX2021-001230-S, funded by MCIN/AEI/10.13039/501100011033, is gratefully acknowledged. Funding for open access charge: Universitat Politècnica de València.

Conflicts of Interest

The authors declare no conflicts of interest.

Data Availability Statement

The data that support the findings of this study are openly available in [Zenodo] at [http://doi.org/10.5281/zenodo.17278409], reference number [17278409].

References

1. H. S. P. Wong and S. Salahuddin, "Memory Leads the Way to Better Computing," *Nature Nanotechnology* 10 (2015): 191–194, https://doi.org/10.1038/nnano.2015.29.

2. Y. Huang, T. Ando, A. Sebastian, M.-F. Chang, J. J. Yang, and Q. Xia, "Memristor-Based Hardware Accelerators for Artificial Intelligence," *Nature Reviews Electrical Engineering* 1 (2024): 286–299, https://doi.org/10.1038/s44287-024-00037-6.

3. Y. Xiao, B. Jiang, Z. Zhang, et al., "A Review of Memristor: Material and Structure Design, Device Performance, Applications and Prospects," *Science and Technology of Advanced Materials* 24 (2023): 2162323, https://doi.org/10.1080/14686996.2022.2162323.

4. F. Aguirre, A. Sebastian, M. Le Gallo, et al., "Hardware Implementation of Memristor-Based Artificial Neural Networks," *Nature Communications* 15 (2024): 1974, https://doi.org/10.1038/s41467-024-45670-9.

5. S.-Y. Kim, H. Zhang, and J. Rubio-Magnieto, "Operating Mechanism Principles and Advancements for Halide Perovskite-Based Memristors and Neuromorphic Devices," *The Journal of Physical Chemistry Letters* 15 (2024): 10087–10103, https://doi.org/10.1021/acs.jpclett.4c02170.

6. J. Bisquert, W. Shim, S.-Y. Kim, and B. Linares-Barranco, "Synaptic Function in Memristor Devices for Neuromorphic Circuit Applications," *Advanced Electronic Materials* 11 (2025): 2400903, https://doi.org/10.1002/aelm.202400903.

7. A. Bou, C. Gonzales, P. P. Boix, Y. Vaynzof, A. Guerrero, and J. Bisquert, "Kinetics of Volatile and Nonvolatile Halide Perovskite Devices: The Conductance-Activated Quasi-Linear Memristor (CALM) Model," *The Journal of Physical Chemistry Letters* 16 (2025): 69–76, https://doi.org/10.1021/acs.jpclett.4c03132.

8. X. Zhang, Y. Wang, X. Zhao, et al., "Halide Perovskite Memristors for Optoelectronic Memory and Computing Applications," *Information & Functional Materials* 1 (2024): 265–281, https://doi.org/10.1002/ifm2.23.

9. K. Biswas, "The Nature of Defect Tolerance in (some) Halide Perovskites," *APL Electronic Devices* 1 (2025): 030901, https://doi.org/10.1063/5.0282710.

10. D.-N. Jeong, J.-M. Yang, and N.-G. Park, "Roadmap on Halide Perovskite and Related Devices," *Nanotechnology* 31 (2020): 152001, https://doi.org/10.1088/1361-6528/ab59ed.

11. S. Lee, J. Son, and B. Jeong, "Ion Dynamics in Metal Halide Perovskites for Resistive-Switching Memory and Neuromorphic Memristors," *Materials Today Electronics* 9 (2024): 100114, https://doi.org/10.1016/j.mtelec.2024.100114.

12. J. Son, M. Lee, A. Sannyal, et al., "Self-Rectifying Resistive Memory With a Ferroelectric and 2D Perovskite Lateral Heterostructure," *ACS Nano* 19 (2025): 10796–10806, https://doi.org/10.1021/acsnano.4c07869.

13. B. W. Zhang, C.-H. Lin, S. Nirantar, et al., "Lead-Free Perovskites and Metal Halides for Resistive Switching Memory and Artificial Synapse," *Small Structures* 5 (2024): 2300524, https://doi.org/10.1002/sstr.202300524.

14. D. Y. Heo and H. Kim, "Lead-Free Halide Perovskite Memristors for Scalable Crossbar Arrays," *Nano Convergence* 12 (2025): 41, https://doi.org/10.1186/s40580-025-00507-z.

15. Z. Feng, J. Kim, J. Min, et al., "Harnessing Earth-Abundant Lead-Free Halide Perovskite for Resistive Switching Memory and Neuromorphic Computing," *Advanced Electronic Materials* 11 (2025): 2400804, https://doi.org/10.1002/aelm.202400804.

16. S.-Y. Kim, D.-A. Park, and N.-G. Park, "Synthetic Powder-Based Thin (<0.1 μm) Cs3Bi2Br9 Perovskite Films for Air-Stable and Viable Resistive Switching Memory," *ACS Applied Electronic Materials* 4 (2022): 2388–2395, https://doi.org/10.1021/acsaelm.2c00201.

17. F. Luo, Y. Wu, J. Tong, F. Tian, and X. Zhang, "Resistive Switching and Artificial Synaptic Performances of Memristor Based on Low-Dimensional Bismuth Halide Perovskites," *Nano Research* 16 (2023): 10108–10119, https://doi.org/10.1007/s12274-023-5411-x.

18. S.-Y. Kim, J.-M. Yang, S.-H. Lee, and N.-G. Park, "A Layered (n-C4H9A layered (n -C 4 H 9 NH 3) 2 CsAgBiBr 7 Perovskite for Bipolar Resistive Switching Memory With a High ON/OFF Ratio," *Nanoscale* 13 (2021): 12475–12483, https://doi.org/10.1039/D1NR03245C.

19. Z. Wu, H. Tüysüz, F. Besenbacher, Y. Dai, and Y. Xiong, "Recent Developments in Lead-Free Bismuth-Based Halide Perovskite Nanomaterials for Heterogeneous Photocatalysis under Visible Light," *Nanoscale* 15 (2023): 5598–5622, https://doi.org/10.1039/D3NR00124E.

20. W. Chen, H. Sun, Y. Jin, H. Yang, Y. He, and X. Zhu, "Preparation of Bismuth-Based Perovskite Cs3Bi2I6Br3 single crystal for X-Ray Detector Application," *Journal of Materials Science: Materials in Electronics* 34 (2023): 496, https://doi.org/10.1007/s10854-023-09897-4.

21. S. Meloni, T. Moehl, W. Tress, et al., "Ionic Polarization-Induced Current–Voltage Hysteresis in CH3NH3PbX3 Perovskite Solar Cells," *Nature Communications* 7 (2016): 10334, https://doi.org/10.1038/ncomms10334.

22. B. Hwang, C. Gu, D. Lee, and J.-S. Lee, "Effect of Halide-Mixing on the Switching Behaviors of Organic-Inorganic Hybrid Perovskite Memory," *Scientific Reports* 7 (2017): 43794, https://doi.org/10.1038/srep43794.

23. Q. Sun, B. Xiao, L. Ji, et al., "Effect of Dimensional Expansion on Carrier Transport Behaviors of the Hexagonal Bi-Based Perovskite Crystals," *Journal of Energy Chemistry* 66 (2022): 459–465, https://doi.org/10.1016/j.jechem.2021.08.052.

24. B.-B. Yu, M. Liao, J. Yang, et al., "Alloy-Induced Phase Transition and Enhanced Photovoltaic Performance: The Case of Cs3Bi2I9−xBrx Perovskite Solar Cells," *Journal of Materials Chemistry A* 7 (2019): 8818–8825, https://doi.org/10.1039/C9TA01978B.

25. Z. Liu, W. Ju, Y. Fang, et al., "In-Plane Adaptive Heteroepitaxy of 2D Cesium Bismuth Halides With Engineered Bandgaps on c -Sapphire," *Advanced Materials* 37 (2025): 2413852, https://doi.org/10.1002/adma.202413852.

26. E. Şen, M. Kaleli, D. A. Aldemir, and H. E. Lapa, "Investigation of MASnIxBr3−x (x = 3, 2, 1, 0) Perovskite Thin Films Produced by Ultrasonic Spray Pyrolysis Method," *Arabian Journal for Science and Engineering* 49 (2024): 10085–10094, https://doi.org/10.1007/s13369-023-08536-8.

27. H. Kim, S. J. Yang, Y.-S. Shim, and C. W. Moon, "A Comprehensive Review of Electrochemical Metallization and Valence Change Mechanisms in Filamentary Resistive Switching of Halide Perovskite-Based Memory Devices," *ACS Applied Materials & Interfaces* 17 (2025): 50122–50141, https://doi.org/10.1021/acsami.5c09862.

28. L. McGovern, G. Grimaldi, M. H. Futscher, et al., "Reduced Barrier for Ion Migration in Mixed-Halide Perovskites," *ACS Applied Energy Materials* 4 (2021): 13431–13437, https://doi.org/10.1021/acsaem.1c03095.

29. H. Bu, C. He, Y. Xu, et al., "Emerging New-Generation Detecting and Sensing of Metal Halide Perovskites," *Advanced Electronic Materials* 8 (2022): 2101204, https://doi.org/10.1002/aelm.202101204.

30. D. Das, D. S. Assi, S. Kazim, V. A. L. Roy, and S. Ahmad, "Decoding halide perovskites for neuromorphic and memristive devices," *Materials Horizons* 12 (2025): 8430–8459, https://doi.org/10.1039/D5MH00534E.

31. G. Rivera-Sierra, P. Ramirez, J. Bisquert, and A. Bou, "Relaxation Time of Multipore Nanofluidic Memristors for Neuromorphic Applications," *Journal of the American Chemical Society* 147 (2025): 17529–17538, https://doi.org/10.1021/jacs.5c04903.

32. W. Guan, S. Long, Q. Liu, M. Liu, and W. Wang, "Nonpolar Nonvolatile Resistive Switching in Cu Doped ZrO_2," *IEEE Electron Device Letters* 29 (2008): 434–437, https://doi.org/10.1109/LED.2008.919602.

33. E. W. Lim and R. Ismail, "Conduction Mechanism of Valence Change Resistive Switching Memory: A Survey," *Electronics* 4 (2015): 586–613, https://doi.org/10.3390/electronics4030586.

34. A. H. Jaafar, L. Meng, T. Zhang, et al., "Flexible Memristor Devices Using Hybrid Polymer/Electrodeposited GeSbTe Nanoscale Thin Films," *ACS Applied Nano Materials* 5 (2022): 17711–17720, https://doi.org/10.1021/acsanm.2c03639.

35. D. Chen, X. Zhi, Y. Xia, et al., "A Digital–Analog Bimodal Memristor Based on CsPbBr3 for Tactile Sensory Neuromorphic Computing," *Small* 19 (2023): 2301196, https://doi.org/10.1002/smll.202301196.

36. C. Gonzales and A. Guerrero, "Mechanistic and Kinetic Analysis of Perovskite Memristors With Buffer Layers: The Case of a Two-Step Set Process," *The Journal of Physical Chemistry Letters* 14 (2023): 1395–1402, https://doi.org/10.1021/acs.jpclett.2c03669.

37. Z. Liu, H. Tang, P. Cheng, et al., "High-Performance and Environmentally Robust Multilevel Lead-Free Organotin Halide Perovskite Memristors," *Advanced Electronic Materials* 9 (2023): 2201005, https://doi.org/10.1002/aelm.202201005.

Supporting Information

Additional supporting information can be found online in the Supporting Information section.

Supporting File: admt70683-sup-0001-SuppMat.docx